Solar Reforming of Methane in a Direct Absorption Catalytic Reactor on a Parabolic Dish: II – Modeling and Analysis*

Russell D. Skocypec, Roy E. Hogan, Jr., and James F. Muir
Sandia National Laboratories
Albuquerque, NM 87185

SAND--90-2946C

DE91 005859

ABSTRACT

The CAtalytically Enhanced Solar Absorption Receiver (CAESAR) experiment was conducted to determine the thermal, chemical, and mechanical performance of a commercial-scale, dish-mounted, direct catalytic absorption receiver (DCAR) reactor over a range of steady state and transient (cloud) operating conditions. The focus of the experiment is on global performance such as receiver efficiencies and overall methane conversion; it was not intended to provide data for code validation. This type of high-temperature chemical reactor volumetrically absorbs concentrated solar energy throughout a catalytic porous absorber matrix volume, promoting heterogeneous reactions with fluid-phase reactant species flowing through the absorber.

A numerical model was previously developed to provide guidance in the design of the absorber. The one-dimensional, planar and steady-state model incorporates the following energy transfer mechanisms: solar and infrared radiation, heterogeneous chemical reaction, conduction in the solid phase, and convection between the fluid and solid phases. A number of upgrades to the model and improved property values are presented here. In particular, the radiative transfer model has been improved by the application of a three-flux technique to more accurately represent the typically conical incidence of solar flux. A spatially varying catalyst loading has been incorporated, convective and radiative properties for each layer in the multi-layer absorber have been determined, and more realistic boundary conditions have been applied.

Model predictions are shown to bound the experimental axial thermocouple data when experimental uncertainties are included. Global predictions are made using a technique in which the incident solar flux distribution is subdivided into flux contour bands. Model predictions for each band are then spatially integrated to provide global predictions such as reactor efficiencies and methane

*This work performed at Sandia National Laboratories supported by the U.S. Department of Energy under Contract DE-AC04-76DP00789.

conversion. Global predictions are shown to compare well with experimental data. Reactor predictions for anticipated operating conditions suggest a further decrease in optical density at the front of the absorber inner disk may be beneficial. The need to conduct code-validation experiments is identified as essential to improve the confidence in the capability to predict large-scale reactor operation.

INTRODUCTION

Solar reforming of methane with carbon dioxide was successfully demonstrated in the CAtalytically Enhanced Solar Absorption Receiver (CAESAR) experiment, which is a joint project between Sandia National Laboratories (Albuquerque, NM) and Deutsche Forschungsanstalt für Luft-und Raumfahrt, DLR, (Stuttgart, Federal Republic of Germany (FRG)). The test reactor, designed to produce approximately 100 $kW_{chemical}$, was installed and tested on a 150 kW, 17 m parabolic dish at the DLR PAN facility in Lampoldshausen, FRG. The CAESAR reactor (see Fig. 1) is the largest solar-driven chemical reactor of any type and is the first to be tested on a dish concentrator. This type of high-temperature chemical reactor volumetrically absorbs concentrated solar energy throughout a catalytic porous absorber matrix volume, promoting heterogeneous reactions with fluid-phase reactant species flowing through the absorber. In this particular reactor, the porous absorber consists of reticulated ceramic impregnated with rhodium catalyst.

A numerical model was previously developed to provide guidance in the design of the absorber and it is discussed in detail in Ref. [1]. Scoping calculations for the thermal and chemical performance of the 100 $kW_{chemical}$ reactor were presented in Ref. [2] for a range of absorber parameters and operating conditions. Predicted performance was based on a prototype absorber and anticipated operating conditions. These predictions were used to provide design recommendations, which were incorporated into the final absorber design for CAESAR. At that time, however, some information necessary to model and evaluate the final design was not available.

The objectives of this paper are to: 1) discuss upgrades of the numerical model described in Ref. [1], 2) compare model predictions with experimental data, 3) indicate the predicted performance potential of these types of reactors under more ideal conditions, and 4) identify research needed to advance the development of these reactors.

EXPERIMENT DESCRIPTION

The objective of the CAESAR experiment is to determine the thermal, chemical, and mechanical performance of a commercial-scale, dish-mounted, direct catalytic absorption receiver (DCAR) reactor over a range of steady state and transient (cloud) operating conditions. Although some thermocouples were placed within the absorber to obtain axial temperature distributions, the focus of the experiment is on global performance such as receiver efficiencies and overall methane conversion. That is, this experiment was not intended to provide data for code validation.

The design and operation of the reactor is described in detail in Ref. [3]. As shown schematically in Fig. 2, the absorber disks (64 cm diameter, 5 cm thick) were fabricated in nine pieces: a 30-cm diameter inner disk and eight outer ring pieces. Two volumetric absorbers were tested; both incorporated the recommendation to decrease the optical density of the absorber at the front (sunlit) side; the second also incorporated the recommendation to tailor the gas mass flux with the incident solar flux distribution. The first absorber had three axial layers (5/10/20 pores-per-inch (ppi) front to back) and was radially uniform, providing a radially uniform flow resistance. The second absorber was radially nonuniform, having the same inner disk but with an outer ring having smaller pore sizes (10/30 ppi front to back), providing increased flow resistance through the outer ring; forcing more mass through regions of higher incident solar flux (the inner disk).

The experimental temperatures were measured with unshielded thermocouples installed in holes drilled from the rear of the absorber. Due to the reticulated nature of the absorber and large radiative fluxes, the thermocouple data require interpretation. That is, the thermocouple data may not directly represent either the solid absorber temperature or the gas temperature. Assuming the thermocouples are not in direct contact with and are not shaded by the absorber, the predicted thermocouple response (calculation of the thermocouple bead temperature in the predicted thermal environment (local radiative, convective fluxes)) can be determined and can be compared with the measured data. If the thermocouple bead had identical properties and reactivity as the solid absorber, its temperature would be the same as the solid temperature. However, since no catalytic chemistry occurs on the thermocouple and its properties are different, the predicted thermocouple response differs. Since this correction is determined

with the predicted thermal conditions (a continuum analysis), discrete effects around each thermocouple that are unknown (e.g., contact with the solid, total shading by a web, etc.) are not accounted for. These discrete effects can significantly affect the actual thermocouple reading.

A cross-array of thermocouples immediately behind the absorber provides the temperature distribution of the gas leaving the absorber. Gas mass flow and composition are controlled by the feed gas controls, and product gas composition is determined by online analyzers and by post-test gas chromatography analysis of collected gas samples.

An accurate knowledge of the solar flux distribution and solar power incident to the receiver is necessary to evaluate receiver performance and to conduct modeling analyses. The incident solar flux distribution was characterized in a series of post-test measurements using the DLR HERMES flux-measurement system for conditions similar to tests of interest (see Ref. [3]). A representative HERMES measurement is shown in Fig. 3.

MODEL DESCRIPTION

The numerical model and solution procedure used to predict reactor performance is described in detail in Ref. [1]. A number of upgrades to the model and improved property values are presented here. In particular, the radiative transfer model has been improved, a spatially varying catalyst loading has been incorporated, convective and radiative properties for each layer in the multi-layer absorber have been determined, and more realistic boundary conditions have been applied. The model, in general, remains the same as presented in Ref. [1].

Briefly, the one-dimensional, planar and steady-state model incorporates the following energy transfer mechanisms: solar and infrared radiation, heterogeneous chemical reaction, conduction in the solid phase, and convection between the fluid and solid phases. It also includes the absorber interaction with the glass reactor window. Energy transfer at the microscale is not explicitly modeled. A continuum (rather than a discrete) approach has been taken. To account for radial variations in incident solar flux and mass flux, several one-dimensional and radially uncoupled problems are solved.

Radiative Transfer: Previously, a two-band, two-flux radiation technique was used to model both the solar and infrared radiative heat

transfer within the absorber. To more accurately represent the typically conical incidence of solar energy, a three-flux technique is used to model radiative transfer in the solar band. Volumetric absorption and radiative flux predictions from the three-flux technique have compared well to those obtained from both the more detailed discrete ordinate method and experiments [4], particularly for concial incidence and anisotropic scattering. The three-flux technique was found to offer a good compromise between accuracy, operational convenience and computation time. The two-flux technique is used for the infrared radiative transfer, which is typically diffuse.

The porous absorber matrix is modeled as a quasi-continuous, nonisothermal, homogeneous medium with transparent boundaries. It is assumed to be an absorbing, emitting, and isotropically scattering medium. Isotropic scattering is assumed since there is a lack of phase function information for radiative transfer within the reticulated material. (Anisotropic phase functions can be incorporated in both techniques.) Any actual anisotropy is accounted for when radiative properties are determined as discussed below. The fluid phase is assumed to be radiatively nonparticipating.

The three-flux technique, as developed in Ref. [4] to more accurately account for the refractive effect at air-water interfaces, is used in this analysis to more accurately account for the typically conical solar flux distribution that occurs in dish concentrators. Additionally, a collimated flux can be included, which is used primarily when analyzing reflectance/transmittance experimental data. The three-flux technique approximates radiative transfer by grouping the noncollimated radiant energy into three isotropic components in the three regions indicated in Fig. 4. The positive-directed hemispherical flux is comprised of two fluxes, q_{s1}^+ and q_{s2}^+, with the boundary between each isotropic region specified by μ_c (=cos(θ_c)). The negative-directed hemispherical flux is represented by q_s^-. For the solar band,

$$\frac{dq_{s1}^+}{dz} = \beta_s \frac{\omega_s(1-\mu_c)-2}{1+\mu_c} q_{s1}^+ + \beta_s \frac{\omega_s(1-\mu_c)}{\mu_c} q_{s2}^+ + \beta_s \omega_s (1-\mu_c) q_s^- + \beta_s \frac{\omega_s}{2}(1-\mu_c) q_{s,coll}, \quad (1)$$

$$\frac{dq_{s2}^+}{dz} = \beta_s \frac{\omega_s \mu_c}{1+\mu_c} q_{s1}^+ + \beta_s \frac{\omega_s \mu_c - 2}{\mu_c} q_{s2}^+ + \beta_s \omega_s \mu_c q_s^- + \beta_s \frac{\omega_s \mu_c}{2} q_{s,coll}, \quad (2)$$

$$\frac{dq_s^-}{dz} = -\beta_s \frac{\omega_s}{1+\mu_c} q_{s1}^+ - \beta_s \frac{\omega_s}{\mu_c} q_{s2}^+ + \beta_s (2-\omega_s) q_s^-$$

$$-\frac{\beta_s\omega_s}{2}q_{s,coll}, \tag{3}$$

$$\frac{dq_{s,coll}}{dz} = -\frac{\beta_s}{\mu_{coll}}q_{s,coll,inc}e^{-\beta_s z/\mu_{coll}}. \tag{4}$$

For the infrared band,

$$\frac{dq_r^+}{dz} = -\beta_r(2-\omega_r)q_r^+ + \beta_r\omega_r q_r^- + 2\sigma\beta_r(1-\omega_r)T_s^4, \tag{5}$$

$$\frac{dq_r^-}{dz} = -\beta_r\omega_r q_r^+ + \beta_r(2-\omega_r)q_r^- - 2\sigma\beta_r(1-\omega_r)T_s^4. \tag{6}$$

At the absorber inlet (sunlit side), the solar and infrared fluxes are specified by considering the interaction with the quartz window. The solar flux from the concentrator (having a rim angle of 32° (μ_c=0.848)) that exits the quartz window and is incident on the absorber is defined as $q^+_{s1,inc}$. For this simulation, both $q_{s,coll,inc}$ and $q^+_{s2,inc}$ are zero. The incident solar flux is assumed uniform over the frontal area being modeled. The boundary conditions for the solar and infrared bands that include interaction with the window are,

$$q^+_{s1}(0) = q^+_{s1,inc} + \rho_{s,w}(1-\mu_c)q_s^-(0), \tag{7}$$

$$q^+_{s2}(0) = \rho_{s,w}\mu_c q_s^-(0). \tag{8}$$

$$q_r^+(0) = \rho_{r,w}q_r^-(0) + \epsilon_{r,w}\sigma T_w^4. \tag{9}$$

At the exit, adiabatic radiative boundary conditions are specified,

$$q^+_{s1}(L) + q^+_{s2}(L) = q_s^-(L), \tag{10}$$

$$q_r^+(L) = q_r^-(L). \tag{11}$$

Properties for radiative transfer in this reticulated material are not well known. The scattering environment requires phase function and scattering cross-section information that, if the absorber was comprised of spheres or cylinders, could be determined using Mie Theory. However, the reticulated nature of the absorber precludes the use of Mie Theory. Additionally, dependent scattering may occur within the absorber, for which the standard radiative transfer equations do not directly apply. Consequently, an empirical approach is taken in which effective solar and infrared properties for the porous absorber matrix are obtained.

Spectrally weighted data from both hemispherical and specular reflectance and transmittance experiments were obtained for various thicknesses of the rhodium-coated absorber illuminated with collimated incident flux. Predictions from the three-flux model

with a collimated incident flux and isotropic scattering were made using different albedos and extinction coefficients and were compared to both the diffuse and specular measured data. The albedo and extinction coefficients for the best fit are taken as the effective radiative properties. These properties include any effects of anisotropic and dependent scattering.

A Beckman 5270 spectrophotometer equipped with an integrating sphere accessory was used to obtain data over the wavelength range 0.265 μm to 2.4 μm. The data are spectrally weighted by the solar energy distribution (air mass 1.5) to obtain the solar-band properties. Reflectance and transmittance properties for the near to mid-infrared wavelength region (2.4 μm to 20.0 μm) were obtained using a Perkin-Elmer Model 1800 FTIR (Fourier Transform Infrared) spectrophotometer that had been modified to use an integrating sphere arrangement [5]. The infrared band data are determined by spectrally weighting the data by the Planck distribution for a blackbody temperature of 1027°C. The effect of varying the blackbody temperature on the infrared band data is small.

Heterogeneous Chemistry and Mass Conservation: The reaction rate expressions and mass conservation equations are presented in Refs. [1,2]. The carbon dioxide reforming reaction is,

$$CH_4 + CO_2 \Longleftrightarrow 2\,CO + 2\,H_2\,, \qquad (12)$$

and the associated water-shift reaction is,

$$CO_2 + H_2 \Longleftrightarrow CO + H_2O\,. \qquad (13)$$

The reaction rates in Ref. [2] are presented in terms of variable weight percent rhodium. Predictions in that reference were presented for an anticipated catalyst loading of 0.2%. Analyses on the absorbers installed in the CAESAR experiments indicated a higher average loading which are not uniform. The pre-test rhodium loading is presented in Table 1.

Energy Conservation: Energy conservation for the solid phase depends on the effective radiative properties, chemical reaction rates, enthalpies of reaction, porosity of the alumina matrix, specific heat transfer area for the alumina matrix, and convective heat transfer coefficient between the solid and fluid phases. For the solid phase,

$$-k(1-\phi)\frac{d^2T_s}{dz^2} = -\left(\frac{dq_{s1}^+}{dz} + \frac{dq_{s2}^+}{dz} - \frac{dq_s^-}{dz} + \mu_{coll}\frac{dq_{s,coll}}{dz} + \frac{dq_r^+}{dz} - \frac{dq_r^-}{dz}\right) - (R_1\Delta H_{R1} + R_2\Delta H_{R2}) - \alpha h_c(T_s - T_f), \qquad (14)$$

The boundary conditions are,

$$-k\frac{dT_s(0)}{dz} = h_c(T_s(0) - T_f(0)), \quad (15)$$

$$-k\frac{dT_s(L)}{dz} = 0. \quad (16)$$

An energy balance on the fluid at $z = 0$ gives the additional condition,

$$(\dot{m}/A)C_{pm}(T_f(0) - T_{f,\text{in}}) - (1 - \phi)h_c(T_s(0) - T_f(0)) = 0, \quad (17)$$

where $T_{f,\text{in}}$ is the fluid temperature at the reactor inlet. These boundary conditions include only surface transfer mechanisms, similar to the approach taken in semitransparent media [6]. Boundary conditions for the radiative fluxes have been specified in Eqs. (7, 8 and 10). The fluid-phase energy balance, thermophysical properties and enthalpic equations are given in Ref. [1]. The specific heat transfer surface area and the convective heat transfer coefficient for each layer was determined from estimations based on optical image analysis (see Ref. [2]) and physical data (porosity, web sizes, etc.). These parameters are listed in Table 1.

Solution Procedure: The equations describing the thermal and chemical conditions in the volumetric solar absorption chemical reactor are formed as a system of fifteen coupled, nonlinear, first-order, ordinary differential equations. The radiative properties, specific heat transfer area, convective heat transfer coefficient and rhodium loading vary for each layer (having different pores-per-inch) in the absorber. Table 1 presents a summary of all property values for each layer in both absorbers. The radiative transfer and energy equations require the boundary conditions for this system of equations to be imposed at both the absorber inlet and the absorber exit. This nonlinear two-point boundary value problem is solved using the SUPOR Q computer code [7], which preserves relative accuracy by reorthonormalizing the solution vectors whenever they begin to lose their numerical linear independence and by the use of an adaptive solution point scheme. The absolute and relative error criteria are 1×10^{-3}.

COMPARISON WITH TEST DATA

As discussed previously, the thermocouple data may not directly represent either the solid absorber temperature or the gas temperature. Assuming the thermocouples are not in direct contact with the absorber, the thermocouple response is determined by performing an energy balance on the thermocouple bead in the predicted thermal environment (local radiative, convective fluxes)).

Table 1: Pre-test Parameter Values

Absorber	Radially Uniform			Radially Nonuniform*	
Layer	1	2	3	1	2
Pores/inch	5	10	20	10	30
Thickness(cm)	2.0	1.73	1.27	2.0	3.0
% Rh loading	0.6	0.3	0.4	0.6	0.4
Radiation					
$\beta_s(m^{-1})$	232.5	280.5	403.5	280.5	564.5
ω_s	0.331	0.286	0.319	0.286	0.524
$\beta_s(m^{-1})$	298.5	359.7	561.5	359.7	807
ω_s	0.537	0.540	0.644	0.540	0.771
Convection					
$\alpha(m^2/m^3)$	600	900	1400	900	1800
h_c (W/m^{2}K)	74	79	100	79	120
k =4.327 W/mK, ϕ=0.85					
Inlet: P_{mix} = 1.0 atm, $T_{f,in}$ = 300 K					
Window: $\rho_{s,w}$ = 0.1, $\rho_{r,w}$ = 0.05, $\epsilon_{r,w}$ = 0.7, T_w = 800 K					
* Outer ring (inner disk same as radially uniform absorber)					

The thermocouple temperature is given by the nonlinear transcendental equation,

$$\sigma\epsilon_{TC}T_{TC}^4 + h_c(T_{TC} - T_f) = \frac{\epsilon_{TC}}{2}(q_{s1}^+ + q_{s2}^+ + q_s^- + \mu_{coll}q_{s,coll} + q_r^+ + q_r^-), \quad (18)$$

where ϵ_{TC} is the thermocouple emissivity and is assumed equivalent to the absorptivity. A Newton-Raphson approach is used to solve for the thermocouple temperature.

Comparison with Axial Temperature Distributions: In order to compare model predictions with experimental thermocouple data, estimations of absorber properties during the test need to be specified. Since the post-test analysis of the uniform absorber indicated substantial changes in the rhodium activity and physical cracking [2], a test that was conducted relatively early in the test sequence was chosen for comparison in the hope that pre-test parameter estimates for the absorber were applicable. Test 1L-B34 was one of the earliest tests for which good (steady-state) data was obtained, although many tests had been conducted prior to this test (approximately 7.6 hours of testing out of a total of 11.5 hours of testing on this absorber). Thus, even though this is one of the earlier tests, it is probable that the absorber had already been altered from pretest conditions.

Three parameter values are believed to have large uncertainties: the solar flux level (recall the nonuniform flux distribution indicated in Fig. 3), the fluid mass flux (due to the annular ring flow entry technique), and the rhodium loading levels (due to nonuniform loading and post-test indications of deactivation). The incident solar flux near the location of the axial thermocouples (center of the absorber) was determined by examining the HERMES flux data. For test 1L-B34 (40 minutes), the incident flux was 525±15 kW/m^2 near the axial thermocouples. If the absorber has a radially uniform flow resistance, the annular fluid inlet with no mixing region will produce a nonuniform radial flow field, with decreased flow toward the centerline. At the centerline, the best estimate for the fluid mass flux is that for uniform flow (0.1075 kg/m^2s) with an estimation that the mass flux near the center could be decreased by up to 20%.

The rhodium activity in each of the three layers in the absorber could range from the pre-test values specified in Table 1 to the post-test values. The measured post-test decrease in reaction rates is accounted for in the model by decreasing the catalyst weight-percent loading levels to: 0.031 for the 5 ppi layer, 0.039 for the 10 ppi layer, and 0.084 for the 20 ppi layer (the degradation was not axially uniform – compare with Table 1). An additional uncertainty is the value for the thermocouple emittance to be used in Eq. (18). The thermocouple emittance during these tests was taken to be 0.85±0.15.

The effect of these parameter uncertainties are considered when comparing the predicted thermocouple response with the thermocouple data. Parameter values that provide an upper bound, a lower bound, and a best estimate for the predicted thermocouple response are listed in Table 2. The best estimate parameters are: average thermocouple emittance, uniform fluid mass flux, average solar flux near the absorber center, and a rhodium loading that gives a predicted exit temperature equal to the measured exit fluid temperatures. This last condition was imposed since the greatest confidence lies in the thermocouple data near the rear of the absorber and in the fluid temperatures (recall the previous discussion regarding discrete effects on the thermocouple data). The comparison of the experimental data with these predicted values are shown in Fig. 5. The thermocouple data is generally bounded by these predictions, and discrete effects are apparent (e.g., the data point at 3.7 cm). The spread between the upper and lower bounds is not constant across the absorber. The corresponding predictions for the solid and fluid temperature distributions are shown in Fig. 6. There is a large difference between the predicted thermocouple response and the predicted solid and fluid temper-

Table 2: Parameter Values

Temperature Estimate	ϵ_{TC}	$\dot{m}/A$ (kg/m^2s)	Rhodium Loading (wt %) Layer 1	Layer 2	Layer 3	$q_{s1,inc}$ (kW/m^2)
Upper	1.0	0.1075	0.6	0.3	0.4	510
Best	0.85	0.1075	0.075	0.0375	0.05	525
Lower	0.7	0.0863	0.031	0.039	0.084	540

atures toward the front of the absorber due to the solar flux. The predicted thermocouple, solid, and fluid temperatures all coalesce toward the rear of the absorber, which is more uniform in temperature. The effect of ϵ_{TC} on the thermocouple temperature decreases as the absorber becomes isothermal (see Eq. (18)).

Figure 7 shows the corresponding methane mole fraction distributions, which are similar in magnitude. The volumetric power distributions for the terms in the energy equation are shown in Fig. 8. The effect of decreasing the optical density toward the front (sunlit) side of the absorber is evident by the deeper penetration into the absorber of the solar energy (i.e., it is more volumetric), relative to that shown in Ref. [2]. This effect is also shown by the solid temperature distributions (Fig. 6). The discrete layer locations can be observed in the chemical power distributions.

Comparison with Global Results: To use the one-dimensional model predictions to provide global results, the nonuniform solar flux distribution must be subdivided into flux contour bands. Model predictions are made for each flux band (using the average incident flux), which are then spatially integrated over the absorber cross-section. (Area-averaging the solar flux is inappropriate due to the nonlinearity of methane conversion with solar flux.) The fluid mass flux is assumed uniform across the absorber. Once the fluid leaves the absorber, the fluid from each flux contour band mixes to produce a uniform exit mixture (no heterogeneous chemistry occurs). Mass and energy balances are performed to obtain the mixture composition and temperature. The thermal and chemical efficiencies and methane conversion are calculated from the exit mixture conditions.

For test 1L-B34, the three-dimensional incident solar flux distribution is shown in Fig. 3, indicating nonuniform illumination conditions. A grey-scale image of the 256x256 pixel HERMES data is shown in Fig. 9. Outlines of the inner disk and outer ring of the absorber are shown. At the center of the image is an

anomaly that is not readily apparent in Fig. 3. A very sharp dropoff in flux values is observed, which occurs at the same pixels in every HERMES flux distribution data file investigated (regardless of the location of the flux image within the data). Since the dropoff in value is extremely sharp and is at the same location in the data files, this anomaly is believed to be caused by bad pixels in the HERMES camera. The affected area is small, so that the effect on this analysis is negligible.

Contours for specified levels are calculated and the contour lines are stored as polygon spline-fit paths. A flux-weighted centroid of the image is determined and is associated with the center of the absorber. An exclusion region is defined for all positions outside a 0.3 m radius from the centroid, so that only the flux that illuminates the 0.3-m radius absorber is analyzed. The polygon areas within all contour paths are determined, from which the appropriate area for each flux band are determined. These areas are used when integrating across the absorber to calculate exit conditions. The flux contour bands (50-150, 150-250, 250-350, 350-450, 450-550, and > 550 kW/m^2) are graphically indicated in Fig. 10 as shaded contours. This indicates the flux distribution that illuminates the absorber.

Table 3 shows the six flux bands, the associated area for each, and the predicted results for each flux band (the incident solar flux for each calculation is taken to be the average of the flux band contour levels). Table 3 indicates the wide range of predicted

Table 3: Predicted Exit Conditions for Test 1L-B34 (40 minutes)

Flux Band (kW/m^2)	Area m^2	X_{CH_4}	X_{CO_2}	X_{CO}	X_{H_2}	X_{H_2O}	T_f(°C)
50 - 150	0.00344	0.446	0.485	0.037	0.028	0.004	481.73
150 - 250	0.02297	0.329	0.354	0.165	0.139	0.013	533.05
250 - 350	0.09114	0.230	0.248	0.270	0.234	0.018	578.19
350 - 450	0.11020	0.154	0.163	0.352	0.310	0.021	622.74
450 - 550	0.0526	0.092	0.096	0.418	0.370	0.024	670.49
> 550	0.00239	0.047	0.045	0.468	0.412	0.028	743.74
Mixture Values:		0.177	0.188	0.328	0.287	0.020	609.98

exit composition and temperature that can be generated by a nonuniform solar flux distribution. An order of magnitude variation in mole fractions and over 250°C difference in temperature are predicted. However, over 70% of the absorber is illuminated by flux levels between 250 and 450 kW/m^2, which is reflected

in the mixture values. Reactor efficiencies are determined from this data. Receiver efficiency, η_r, is the percent of incident solar power transferred to the fluid phase as the total mixture enthalpy change (including both chemical and sensible enthalpy). Chemical efficiency, η_{ch}, is the percent of incident solar power transferred to the fluid phase as chemical enthalpy change. Methane conversion is the percent of methane entering the reactor that is converted. For test 1L-B34, 40 minutes, η_r= 71.9%, η_{ch}=48.2%, and 46.5% of the methane is converted. This compares well to the experimental data listed in Table 1 of Ref. [3] (entry identified as 105.7 kW solar power), which specifies η_r=79.3%, η_{ch}=50.7%, and 45.9% methane conversion.

Predictions for Anticipated Conditions: To evaluate the radially tailored absorber (inner disk and outer ring) design under conditions that were anticipated for these tests, predictions were made for the solar flux levels and mass flux levels specified for Case 2B in Ref. [2]. For the inner disk, $q_{s1,inc}$= 1912 kW/m^2, $\dot{m}/A$= 0.2538 kg/m^{2}s; and for the outer ring, $q_{s1,inc}$= 317 kW/m^2, $\dot{m}/A$= 0.042 kg/m^{2}s. The fluid mixing analysis at the absorber exit identified above is applied. The pre-test parameter values specified in Table 1 for the nonuniform absorber are used.

The predicted axial temperature and methane mole fraction distributions for both the inner disk and outer ring are presented in Fig. 11. Thermal and chemical conditions between the inner disk and outer ring are more uniform than predicted conditions for a non-tailored absorber. The inner disk solid reaches an unacceptably high temperature, which is caused in part by the unexpectedly high rhodium loading indicated in Table 1. The high catalyst loading both decreases the front surface temperature due to the endothermic chemical activity and generates a thermal maxima within the absorber due to rapid reactant depletion. The effect of increased catalyst loading was also observed in Ref. [2]. The effect of decreasing the optical density toward the front of the absorber relative to that in the prototype absorber in Ref. [2] is evident in Fig. 11. The optical density in the inner disk should be further decreased, if practical. Predicted reactor efficiencies are: η_r= 71.5%, η_{ch}=46.7%, and 99.1% of the methane is converted. Relative to the reactor efficiencies calculated for test 1L-B34, a significant increase in methane conversion is obtained with similar receiver and chemical efficiencies.

DIRECTION FOR FUTURE WORK

The most pressing need is to conduct laboratory-scale experiments under relatively well-controlled conditions with sufficient diagnostics so that comparisons can be made with code predictions. That is, code validation experiments need to be conducted, producing greater confidence in our predictive capability for larger-scale experiments. Additional needs have been identified, but at this time they are not as crucial to the development of these reactors.

SUMMARY

A number of upgrades to the previous numerical model and improved property values have been presented. In particular, the radiative transfer model has been improved by the application of a three-flux technique to more accurately represent the typically conical incidence of solar flux. A spatially varying catalyst loading has been incorporated, convective and radiative properties for each layer in the multi-layer absorber have been determined, and more realistic boundary conditions have been applied.

Model predictions are shown to bound the experimental axial thermocouple data when experimental uncertainties are included. Global predictions are made using a technique in which the incident solar flux distribution is subdivided into flux contour bands. Model predictions for each band are then spatially integrated to provide global predictions such as reactor efficiencies and methane conversion. Global predictions are shown to compare well with experimental data. Reactor predictions for anticipated operating conditions suggest a further decrease in optical density at the front of the absorber inner disk may be beneficial.

The need to conduct code-validation experiments is identified as essential to improve the confidence in the capability to predict large-scale reactor operation.

ACKNOWLEDGEMENTS

The authors gratefully acknowledge the assistance of M. W. Glass from Sandia National Laboratories for image processing and contour quantification, and Reiner Buck from DLR-ITT for conducting the CAESAR tests and providing experimental data.

NOMENCLATURE

A	reactor frontal area (m^2)
C_{pm}	constant-pressure specific heat of mixture (J/kg K)
h_c	convective heat transfer coefficient (W/m^2K)
ΔH_{R1}	enthalpy of reaction for reforming reaction (J/kmol CH_4)
ΔH_{R2}	enthalpy of reaction for water-shift reaction (J/kmol CO_2)
k	thermal conductivity (W/mK)
L	geometric thickness of absorber (m)
$\dot{m}$	mixture mass flow rate (kg/s)
P_{mix}	reactor pressure (atm)
$q_r^{\pm}$	positive- or negative-directed infrared hemispherical radiative flux (W/m^2)
q_{s1}^{+}	positive-directed solar flux within region 1
q_{s2}^{+}	positive-directed solar flux within region 2
q_s^{-}	negative-directed solar flux
R_1	reaction rate for reforming reaction ((kmol of CH_4 consumed)/(s m^3))
R_2	reaction rate for water-shift reaction ((kmol of CO_2 consumed)/(s m^3))
T	temperature (K)
$w_{\%}$	weight percent of rhodium catalyst
X_i	mole fraction of species i
z	geometric distance into the absorber (m)

Greek

α	matrix specific convective heat transfer area (m^2/m^3)
β	extinction coefficient (m^{-1})
ϵ	emittance
η_{ch}	chemical efficiency (%)
η_r	reactor efficiency (%)
θ	angle from normal
θ_c	angle from normal defining regions for q_{s1}^{+} and q_{s2}^{+}
μ_c	$\cos\theta_c$
μ_{coll}	$\cos\theta_{coll}$
ρ	reflectance
σ	Stefan-Boltzmann constant ($W/(m^2\ K^4)$)
ϕ	porosity, =(void volume)/(matrix volume)
ω	single scattering albedo

Subscripts

TC	thermocouple
coll	collimated
inc	incident
in	inlet

f	fluid
r	infrared band
s	solar band, solid
w	window

REFERENCES

1) Hogan, R. E., Jr., and Skocypec, R. D., "Analysis of Catalytically Enhanced Solar Absorption Chemical Reactors: I - Basic Concepts and Numerical Model Description," *Solar Energy Technology - 1989*, ASME SED-Vol. 8, 31-37, 1989.

2) Skocypec, R. D., and Hogan, R. E., Jr., "Analysis of Catalytically Enhanced Solar Absorption Chemical Reactors: II - Predicted Characteristics of a 100 $kW_{chemical}$ Reactor," *Solar Energy Technology - 1989*, ASME SED-Vol. 8, 39-47, 1989.

3) Muir, J. F., Hogan, R. E., Skocypec, R. D., and Buck, R., "Solar Reforming of Methane in a Direct Absorption Catalytic Reactor on a Parabolic Dish: I - Test and Analysis," 1991 ASME-JSME International Solar Energy Conference, Reno, Nevada, Accepted.

4) Incropera, F. P., and Houf, W. G., "A Three-Flux Method for Predicting Radiative Transfer in Aqueous Suspensions," *J. Heat Transfer*, Vol. 101, 496-501, 1979.

5) Tardy, H. L., and Dunn, R. G., "Spectral Hemispherical Reflectometer for the Mid-Infrared," *Sandia National Laboratories Report*, SAND86-2886J, 1987.

6) Viskanta, R., and Anderson, E. E., Heat Transfer in Semitransparent Solids, in Advances in Heat Transfer, Vol. 11, T. F. Irvine and J. P. Hartnett, Eds., 385-391, 1975.

7) Scott, M. R. and Watts, H. A., "Computational Solution of Nonlinear Two-Point Boundary-Value Problems," *Proceedings of the Fifth Symposium on Computers in Chemical Engineering*, Czechoslovakia, October 8-9, 17-27, 1977.

Figure 1. Schematic of CAESAR reactor.
Figure 2. Schematic of CAESAR absorbers.
Figure 3. Solar incident flux distribution for Test 1L-B34.
Figure 4. Coordinate system for three-flux radiative transfer technique.
Figure 5. Comparison of experimental thermocouple data (test 1L-B34, 40 minutes) with predicted thermocouple response.
Figure 6. Predicted axial distributions of solid and fluid temperature for test 1L-B34, 40 minutes.
Figure 7. Predicted axial distributions of methane mole fraction for test 1L-B34, 40 minutes.
Figure 8. Predicted axial distributions of volumetric power for test 1L-B34, 40 minutes.
Figure 9. Grey-scale image of solar incident flux distribution for test 1L-B34. Inner disk and outer ring areas identified.
Figure 10. Contour bands for solar flux incident on absorber, test 1L-B34.
Figure 11. Predicted axial distributions of temperature and methane mole fraction for inner disk and outer ring with anticipated operating conditions.

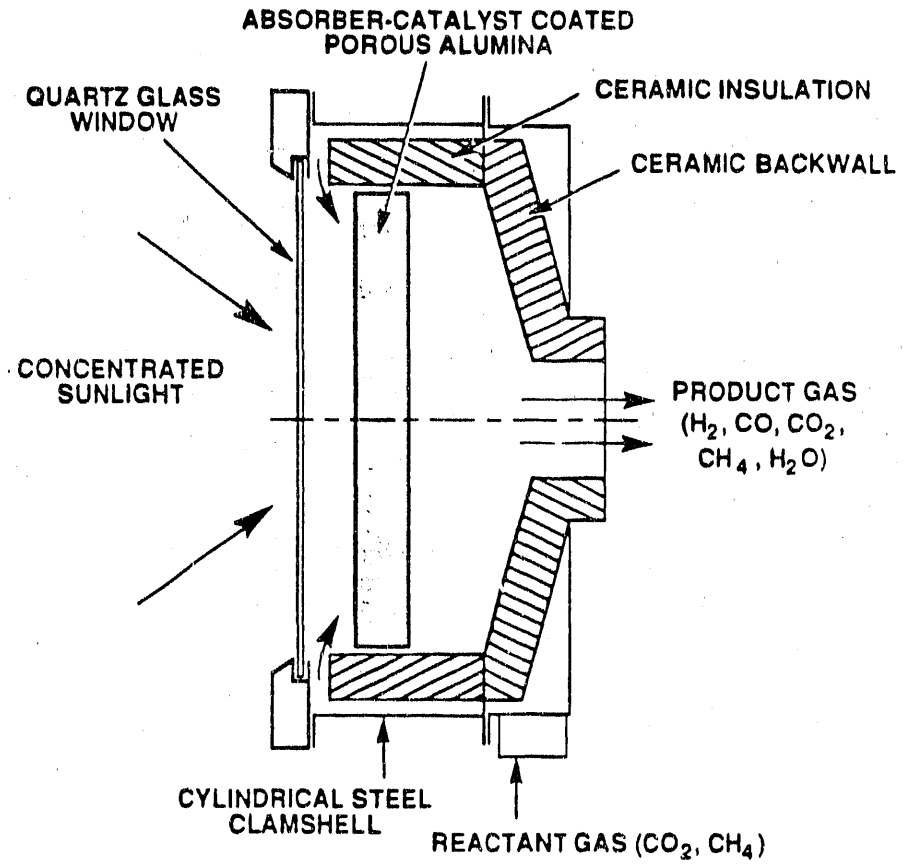
ABSORBER-CATALYST COATED
POROUS ALUMINA
QUARTZ GLASS
WINDOW
CERAMIC INSULATION
CERAMIC BACKWALL
CONCENTRATED
SUNLIGHT
PRODUCT GAS
(H_2, CO, CO_2,
CH_4, H_2O)
CYLINDRICAL STEEL
CLAMSHELL
REACTANT GAS (CO_2, CH_4)

FIGURE 1.

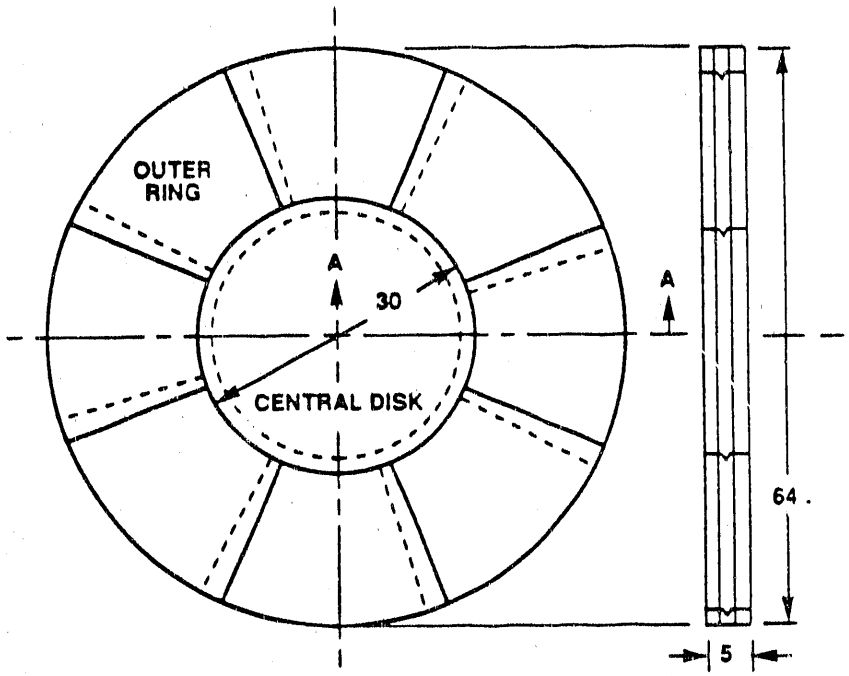

SECTION A-A

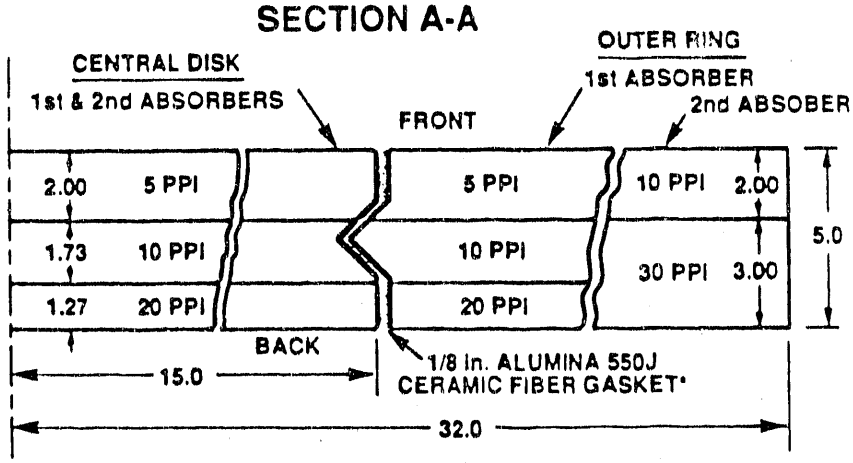

*ALL "V" TONGUE & GROOVE JOINTS TRIANGULAR IN CROSS SECTION:
1.096 BASE x 0.953 HEIGHT

DIMENSIONS IN CM

FIGURE 2

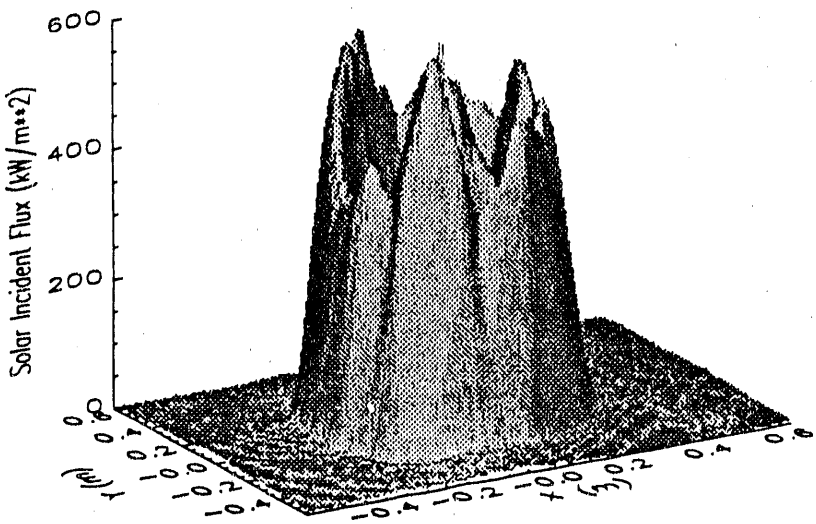
Solar Incident Flux (kW/m**2)
600
400
200
0
0.4
0.2
-0.0
-0.2
-0.4
(m)
-0.4
-0.2
-0.0
0.2
0.4
(m)

FIGURE 3

Draft Figure

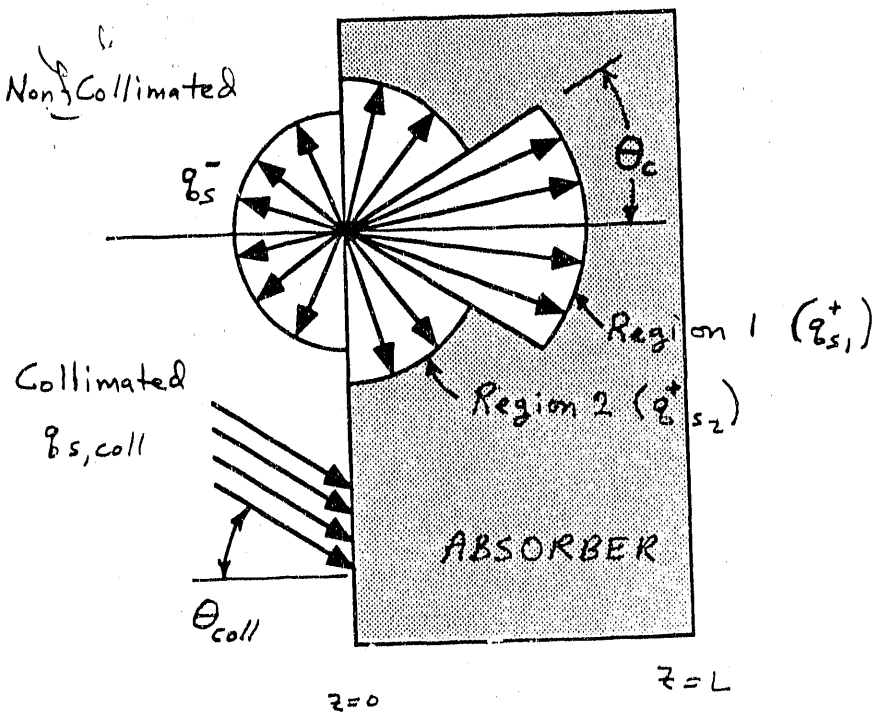

FIGURE 4

FIGURE 5

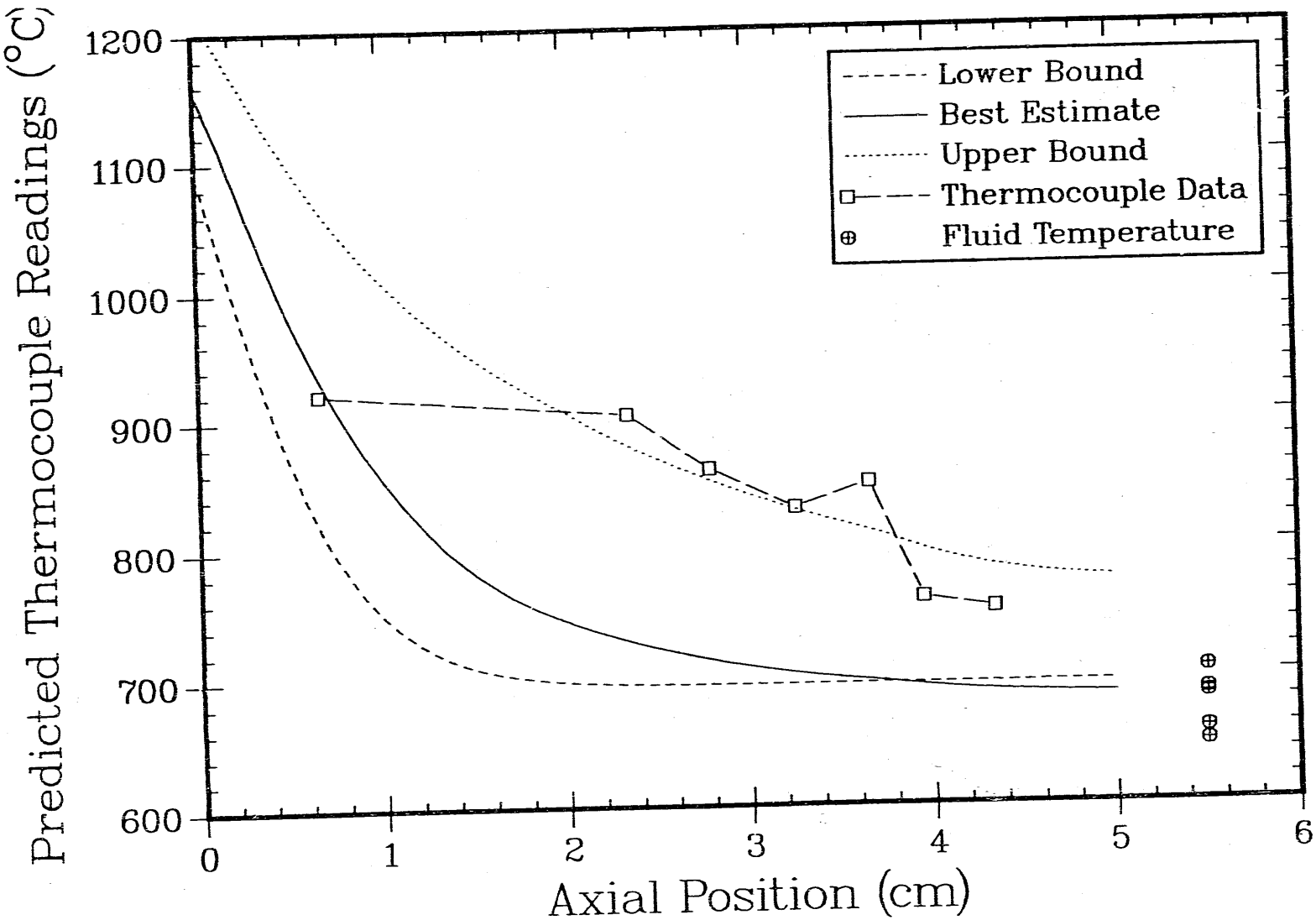

C1L-B34-40-FIG.RST

FIGURE 6

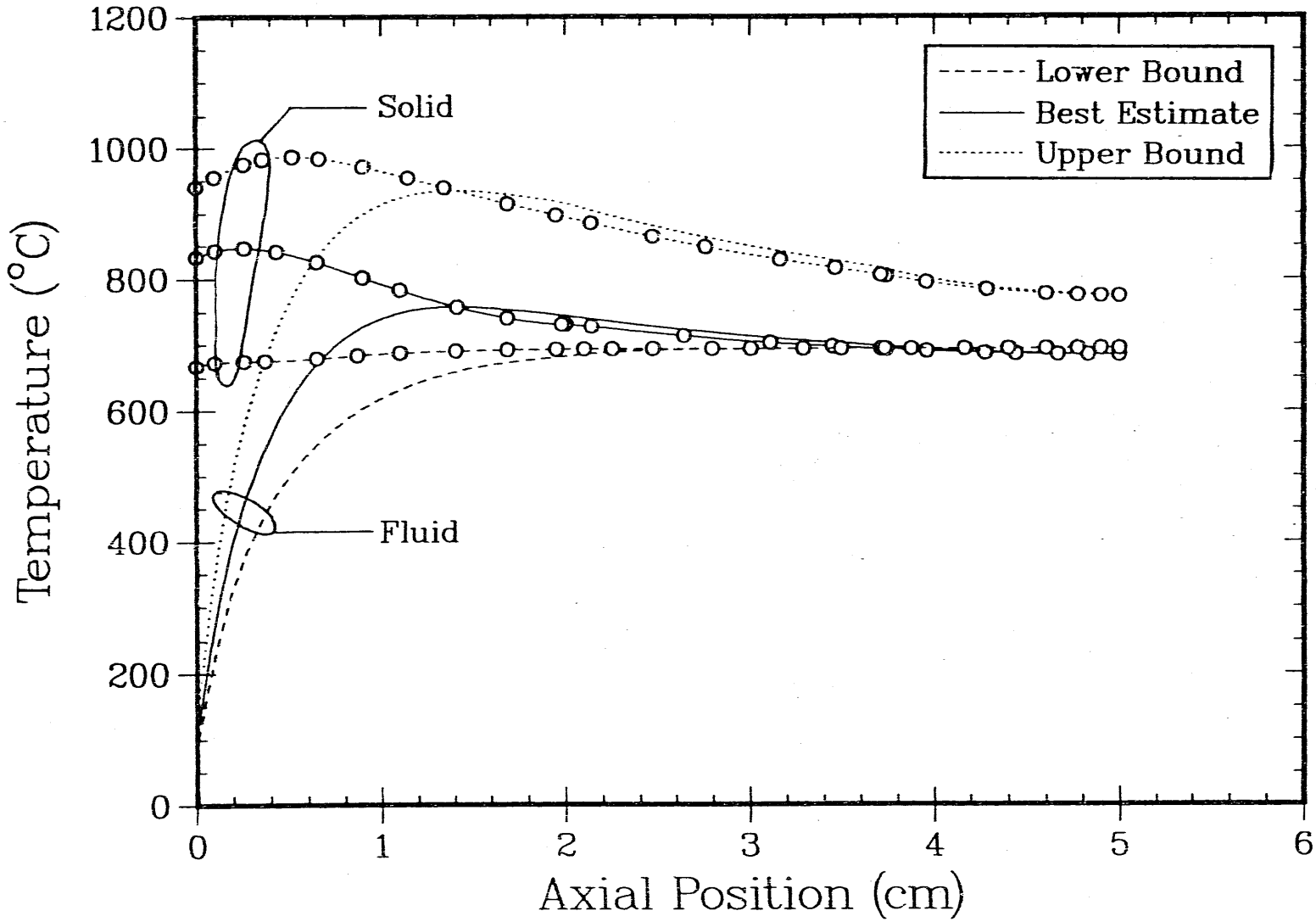

C1L-B34-40-FIG.RST

FIGURE 7

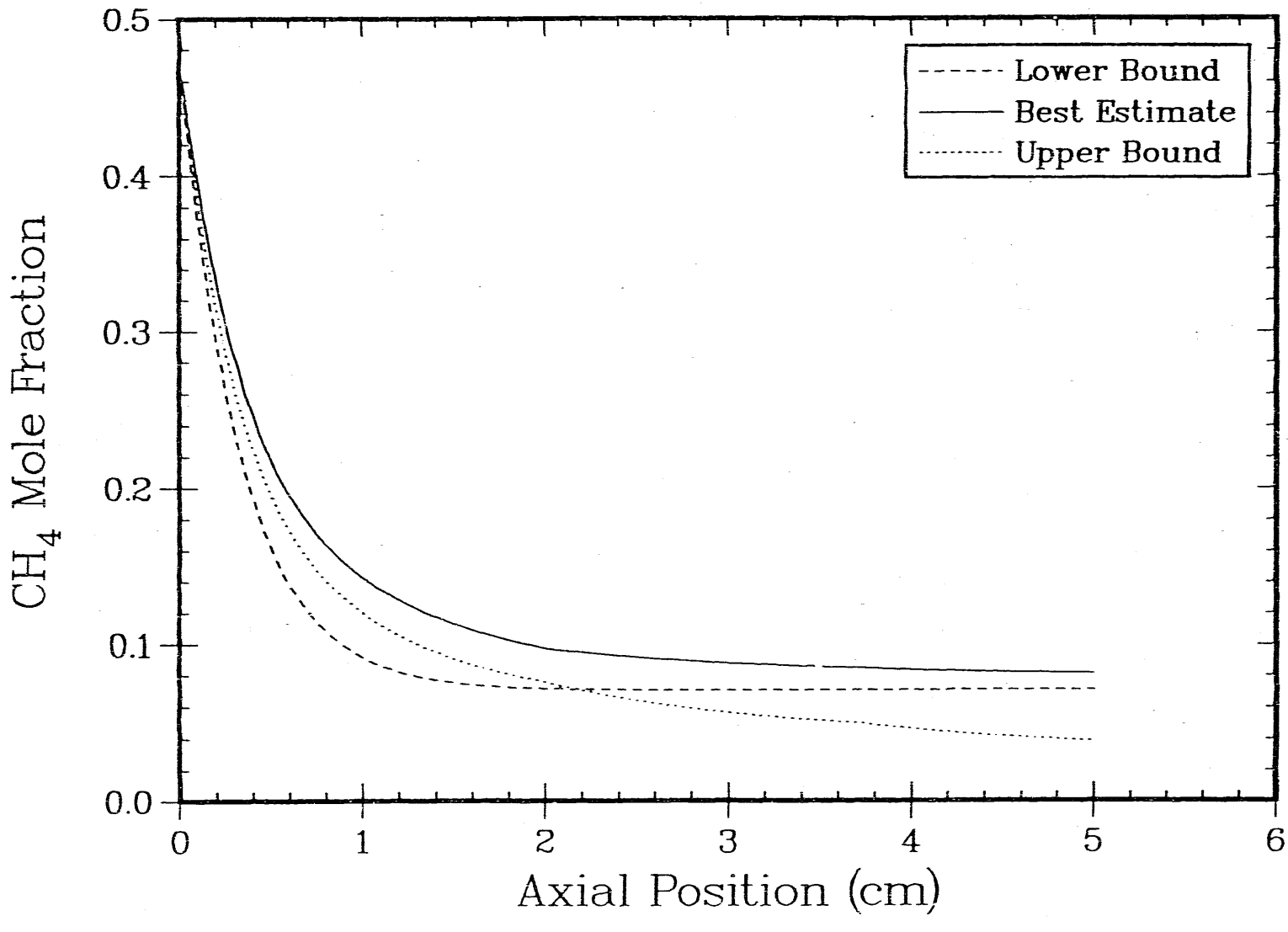

~~CIL-B34-40-FIG.RST~~

FIGURE 8

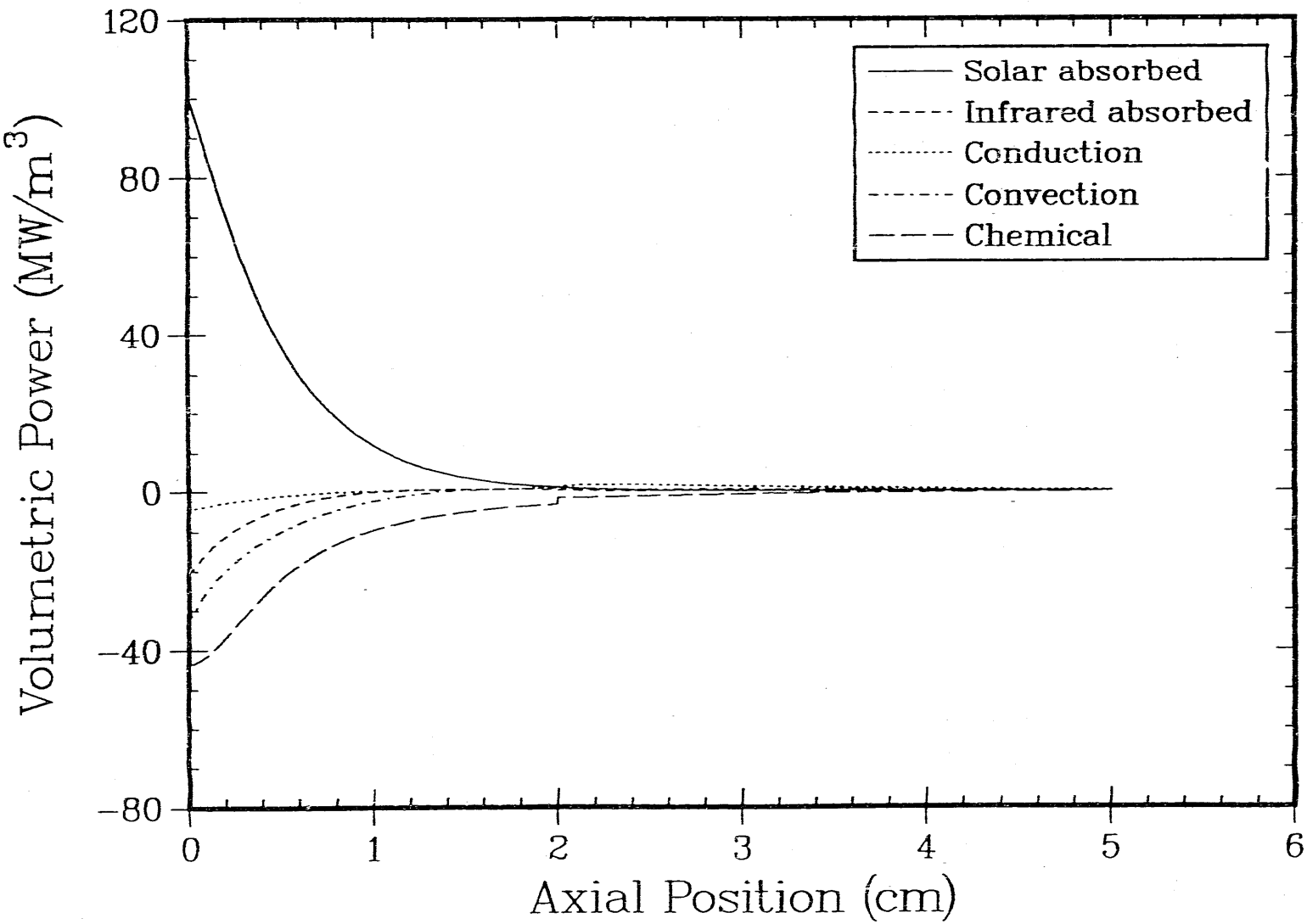

~~C1L-B34-40-FIG.RST~~

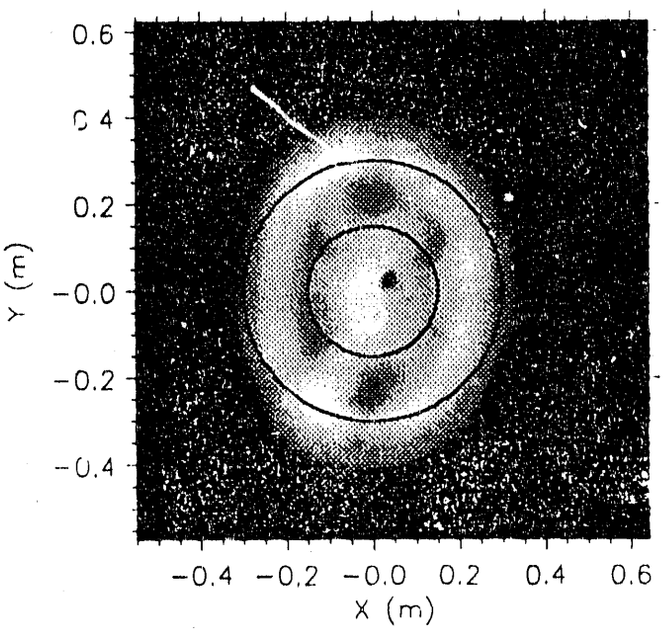

FIGURE 9

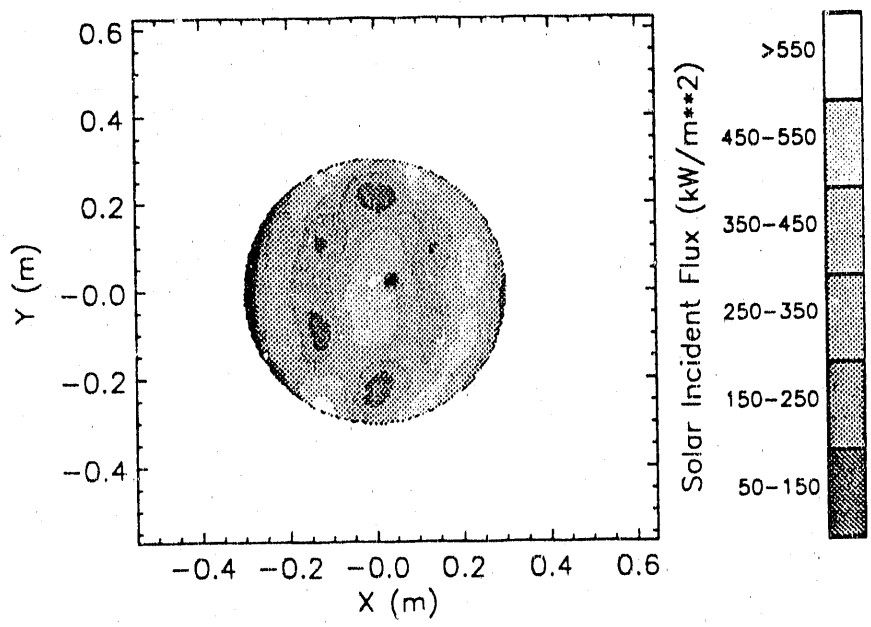
0.6
0.4
0.2
−0.0
−0.2
−0.4
Y (m)
−0.4 −0.2 −0.0 0.2 0.4 0.6
X (m)
Solar Incident Flux (kW/m**2)
>550
450−550
350−450
250−350
150−250
50−150

FIGURE 10

FIGURE 11

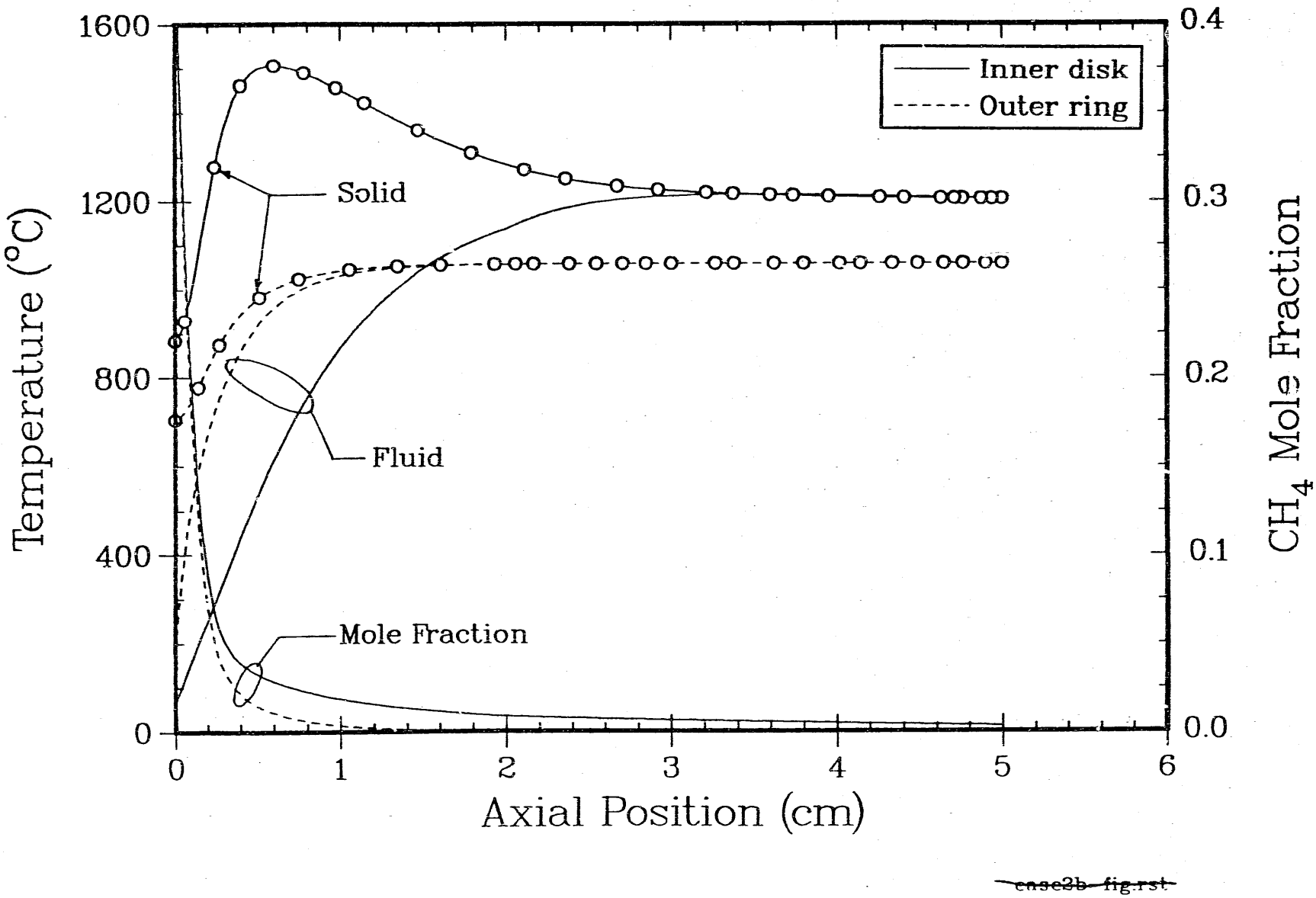
Temperature (°C)
1600
1200
800
400
0
0
1
2
3
4
5
6
Axial Position (cm)
0.4
0.3
0.2
0.1
0.0
CH_4 Mole Fraction
Inner disk
Outer ring
Solid
Fluid
Mole Fraction
case3b_fig.rst

END

DATE FILMED

02 / 08 / 91